

2012

Mathematical Model Development of Super-Resolution Image Wiener Restoration

Amr H. Yousef
Old Dominion University

Jiang Li
Old Dominion University, jli@odu.edu

Mohammad A. Karim
Old Dominion University

Follow this and additional works at: https://digitalcommons.odu.edu/ece_fac_pubs



Part of the [Bioimaging and Biomedical Optics Commons](#), [Electrical and Computer Engineering Commons](#), and the [Theory and Algorithms Commons](#)

Original Publication Citation

Yousef, A., Li, J., & Karim, M. (2012). Mathematical model development of super-resolution image Wiener restoration. *Optical Engineering*, 51(3), 1-12, Article 037007. <https://doi.org/10.1117/1.OE.51.3.037007>

This Article is brought to you for free and open access by the Electrical & Computer Engineering at ODU Digital Commons. It has been accepted for inclusion in Electrical & Computer Engineering Faculty Publications by an authorized administrator of ODU Digital Commons. For more information, please contact digitalcommons@odu.edu.

Optical Engineering

SPIEDigitalLibrary.org/oe

Mathematical model development of super-resolution image Wiener restoration

Amr Yousef
Jiang Li
Mohammad A. Karim

Mathematical model development of super-resolution image Wiener restoration

Amr Yousef

Jiang Li

Mohammad A. Karim

Old Dominion University

4901 Hampton Boulevard

Norfolk, Virginia, 23508

E-mail: aabde008@odu.edu

Abstract. In super-resolution (SR), a set of degraded low-resolution (LR) images are used to reconstruct a higher-resolution image that suffers from acquisition degradations. One way to boost SR images visual quality is to use restoration filters to remove reconstructed images artifacts. We propose an efficient method to optimally allocate the LR pixels on the high-resolution grid and introduce a mathematical derivation of a stochastic Wiener filter. It relies on the continuous-discrete-continuous model and is constrained by the periodic and nonperiodic interrelationships between the different frequency components of the proposed SR system. We analyze an end-to-end model and formulate the Wiener filter as a function of the parameters associated with the proposed SR system such as image gathering and display response indices, system average signal-to-noise ratio, and inter-subpixel shifts between the LR images. Simulation and experimental results demonstrate that the derived Wiener filter with the optimal allocation of LR images results in sharper reconstruction. When compared with other SR techniques, our approach outperforms them in both quality and computational time. © 2012 Society of Photo-Optical Instrumentation Engineers (SPIE). [DOI: 10.1117/1.OE.51.3.037007]

Subject terms: super-resolution; aliasing; restoration; continuous-discrete-continuous; signal-to-noise ratio; subpixel shifts.

Paper 111329P received Oct. 24, 2011; revised manuscript received Dec. 23, 2011; accepted for publication Jan. 6, 2012; published online Apr. 2, 2012.

1 Introduction

Developments and challenges in super-resolution (SR) algorithms have attracted many researchers in recent years due to the high demand on its many applications. SR mainly aim to reconstruct an image with a higher resolution from a set of degraded sequence of images that have similar but no identical looks to the captured scene that falls within the acquisition device field of view (FOV).¹ The applications of SR are many, including medical imaging, military surveillance, and remote sensing in which a long observing distance to an object typically reduces the quality of the extracted features in the acquired images.^{2,3} Most SR approaches consist of three main steps: registration, reconstruction, and restoration.

Registration is a process of aligning several images to a reference one. Registration with subpixel accuracy is essential in reconstructing high-resolution (HR) images with enhanced visual quality and minimum unwanted artifacts.⁴ The subpixel registration techniques can be classified into four types: (1) correlation interpolation, (2) intensity interpolation, (3) differential interpolation, and (4) phase correlation.

In correlation interpolation, a discrete correlation function between two images is calculated and interpolated, and the translation is obtained by searching for the maximum of the correlation function. In intensity interpolation, parts of the reference image are selected and interpolated according to the subpixel accuracy required, and a search is conducted over these parts with the unregistered image.⁵ The idea behind differential interpolation is to relate the difference between two consecutive frames to the spatial intensity

gradient of the first image.⁵ Phase-correlation techniques are based on the idea that phase of the cross power-spectrum between two images contains most information of the relative displacement between them. Guizar-Sicairo et al.⁶ proposed one of the most efficient and reliable subpixel registration algorithms based on the phase-correlation technique to estimate the shifts between two images within a subpixel accuracy.⁷

Image reconstruction is a method of reconstructing HR images by incorporating the available different registered low-resolution (LR) pixels to estimate the missing pixels on the HR grid. In most cases, the registered LR pixels are irregularly distributed over the HR grid. Popular techniques for image reconstruction² are nearest-neighbor interpolation, bilinear interpolation, cubic spline interpolation, and piecewise cubic convolution.⁸

Image restoration is a method of correcting the reconstructed HR image from degraded LR images with blurring, aliasing, and noise.⁹ Popular restoration methods are inverse filters, least square filters, and iterative approaches.^{2,10} There are many SR algorithms, and they can be divided into two categories: spatial domain approaches and spatial frequency domain approaches.⁴

Frequency domain approaches include reconstruction via aliasing removal, recursive least squares filters and multichannel sampling theorem-based techniques.⁴ Spatial domain approaches include nonuniform interpolation, algebraic filtered back projection, probabilistic methods like maximum likelihood (ML) estimation, and maximum a posteriori (MAP) based algorithms, projection onto convex set (POCS), hybrid ML/MAP/POCS methods and Tikhonov-Arsenin regularized methods.⁴

Nonuniform approaches are the simplest ones. Alam et al.¹¹ proposed a method to reconstruct a HR infrared image from a set of randomly shifted LR infrared frames and used a weighted nearest-neighbor approach to estimate missing pixels on the HR grid and finally restore the reconstructed image using the traditional Wiener filter.¹² Ur and Gross¹³ used a framework based on the multichannel sampling theorem followed by a deblurring step to reconstruct the SR image. Komatsu et al.¹⁴ proposed a very high-definition (VHD) imaging system using multiple different cameras with high signal-to-noise ratio. Shah and Zakhor¹⁵ proposed a method to enhance images extracted from a video sequence by compensating for inaccurate motion estimation. Nguyen and Milanfar¹⁶ developed an interpolation-restoration method based on wavelets theory to reconstruct SR images.

Tsai and Huang¹⁷ proposed one of the earliest frequency domain SR approaches. They utilized the shift property of the Fourier transform and related the aliased LR images to an ideal image. Kim et al.^{18,19} applied this approach to blurred and noisy images and restored the reconstructed high-resolution image using the Tikhonov regularization.²⁰ Sauer and Allebach²¹ used the POCS method to reconstruct a HR image from LR images based on the assumption that these LR images are not affected by any blur. Stark and Oskoui²² extended the POCS technique to noiseless blurry images and combined interpolation and restoration in one step. Tekalp et al.²³ extended the idea of POCS to reconstruct a HR image from a sequence of LR images that are affected by motion blur (non-zero aperture time). Irani and Peleg²⁴ developed a SR reconstruction approach based on iterative back projection that is used in tomography to minimize the difference between simulated LR images and actual LR images until a predefined error criterion is reached. Nguyen et al.²⁵ used the conjugate gradient method to solve the Tikhonov regularized SR problem by using efficient block circulant preconditions. Farsui et al.²⁶ used the L_1 norm minimization to reduce errors in blur and inter-LR subpixel shifts estimations. Elad and Feuer^{27,28} combine ML, MAP, and POCS approaches into a hybrid method to reconstruct SR image from a set of blurred, noisy, and undersampled images.

In this paper, we revisit the Wiener filter and extend it for the general SR problem. Although, the Wiener filter has been

discussed throughout literatures, our formulation for the SR problem is quite different. The traditional developments of this filter are for a single-image restoration and are based on the assumption that the continuous-discrete-continuous (CDC) model is constrained only by blurring and noise and ignores the insufficient sampling in the image-gathering process. Consequently, it will not actually minimize the mean square error of the reconstructed image. Our work is an extension to the Wiener filter developed by Carl et al.²⁹ that we extend for addressing the SR problem. Also, it is similar to the one given by Jiang et al.² for microscanning reconstruction in which the subpixel shifts between the individual scans are known and follow a uniform pattern. In our developments we extend this filter for the general SR problem where the subpixel shifts are unknown and random. Also, our derivation indicates periodic and nonperiodic frequency interrelationships between different CDC parameters in addition to highlighting the decomposed output components that result from aliasing, blur, and noise encountered during the image-acquisition, intermediate processing, and image display processes. We formulate the Wiener filter as a function of the average signal-to-noise ratio of the CDC system and assume that the LR frames are well registered using one of the most efficient subpixel registration algorithms⁶ and the LR pixels are optimally allocated to the HR grid.³⁰

The rest of this work is organized as follows: In Sec. 2, we describe the LR images formulation. In Sec. 3, we discuss briefly the optimum allocation of LR pixels on the HR grid. In Sec. 4, we derive the stochastic Wiener filter. Section 5 presents our simulation results, and we conclude the paper in Sec. 6.

2 Low Resolution Image Formulation

Figure 1 details our super-resolution CDC-based system components. It represents most of the degradations including blur, noise, and aliasing that are encountered during the image gathering, image reconstruction, and image display processes.

- The blur results from convolving the continuous input scene with spatial shift invariant lowpass filter that represents the spatial frequency response (SFR) of the image-gathering optical lens. In addition, blur

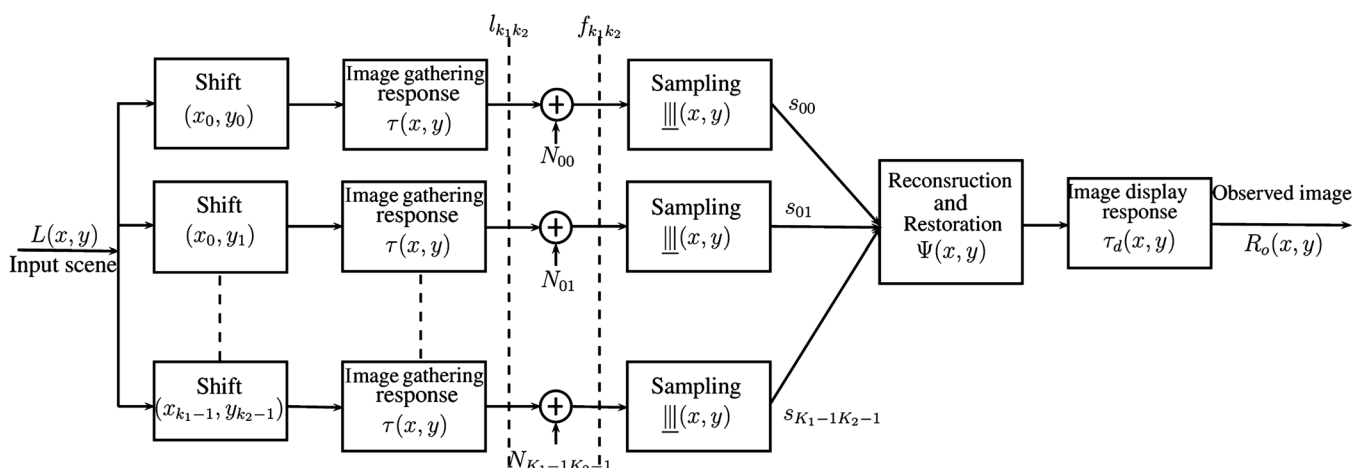


Fig. 1 Complete continuous-discrete-continuous SR reconstruction model.

also occurs when the optical system is out of focus or there is a relative motion between camera and the original scene, and sometimes it is caused by atmospheric turbulence in the case of remote-sensing images.¹⁰

- The additive noise results from image gathering photo-detectors or quantization artifacts. Typically, the noise is white, i.e., spatially uncorrelated. Sometimes, images and noise are correlated especially when noise is multiplicative instead of additive, or the image gathering is nonlinear. For simplicity, noise is modeled as additive white noise.
- The aliasing results from sampling beyond the Nyquist sampling rate causing high frequencies in the scene to fold back into the low-frequencies band. The aliasing causes certain visual artifacts inside the captured images such as jagged lines, spurious highlights, and repeated patterns.¹⁰

For the $k_1 k_2$ th LR frame, the image-gathering device transforms the continuous input scene $L(x, y)$ into discrete signal $s_{k_1 k_2}(x, y)$ as defined by:

$$s_{k_1 k_2}(x, y) = f_{k_1 k_2}(x, y) \underset{\sim}{\parallel} \parallel(x, y) = [L(x - x_{k_1}, y - y_{k_2}) * \tau_{k_1 k_2}(x, y) + N_{k_1 k_2}(x, y)] \underset{\sim}{\parallel} \parallel(x, y), \quad (1)$$

where $\tau_{k_1 k_2}(x, y)$ is the spatial response of the image acquisition device, $N_{k_1 k_2}(x, y)$ is the additive photo-detector noise, the symbol $*$ denotes spatial convolution, and x_{k_1} and y_{k_2} are the subpixel shifts in the x - and y - directions, respectively. The sampling function

$$\underset{\sim}{\parallel} \parallel(x, y) = \sum_m \sum_n \delta(x - m, y - n) \quad (2)$$

denotes sampling on a rectangular grid with unit sampling intervals and $\delta(x, y)$ is the Dirac delta function. The Fourier transform of Eq. (1) gives the spatial frequency representation of the discrete signal $\tilde{s}_{k_1 k_2}$ as defined by:

$$\tilde{s}_{k_1 k_2}(\nu, \omega) = \hat{f}_{k_1 k_2}(\nu, \omega) * \underset{\sim}{\parallel} \parallel(\nu, \omega) = \sum_m \sum_n [\hat{L}(\nu - m, \omega - n) \hat{\tau}_{k_1 k_2}(\nu - m, \omega - n) \times \exp\{-i2\pi[x_{k_1}(\nu - m) + y_{k_2}(\omega - n)]\} + \hat{N}_{k_1 k_2}(\nu - m, \omega - n)], \quad (3)$$

where $\hat{L}(\nu, \omega)$ and $\hat{N}_{k_1 k_2}(\nu, \omega)$ are Fourier transforms of the input scene and the photo-detector noise, respectively, $\hat{\tau}_{k_1 k_2}(\nu, \omega)$ is the spatial frequency response (SFR) of the image acquisition device, the function

$$\underset{\sim}{\parallel} \parallel(\nu, \omega) = \sum_m \sum_n \delta(\nu - m, \omega - n) = \delta(\nu, \omega) + \underset{\sim}{\parallel} \parallel_s(\nu - m, \omega - n) \quad (4)$$

is the Fourier transform of the sampling function and $\underset{\sim}{\parallel} \parallel(\nu, \omega)$ accounts for the sampling sidebands. The associated sampling band is defined as:

$$\hat{B} = \left[(\nu, \omega); |\nu| \leq \frac{1}{2}, |\omega| \leq \frac{1}{2} \right]. \quad (5)$$

The symbol tilde “ \sim ” is used instead of the symbol caret “ $\hat{\cdot}$ ” whenever the corresponding Fourier transformed function is periodic in the spatial frequency domain. Eq. (3) can be rewritten as

$$\tilde{s}_{k_1 k_2}(\nu, \omega) = \hat{L}(\nu, \omega) \hat{\tau}_{k_1 k_2}(\nu, \omega) \exp[-i2\pi(x_{k_1} \nu + y_{k_2} \omega)] + \hat{N}_a(\nu, \omega) + \tilde{N}_{k_1 k_2}(\nu, \omega), \quad (6)$$

where

$$\hat{N}_a(\nu, \omega) = \sum_{m \neq 0} \sum_{n \neq 0} \hat{L}(\nu - m, \omega - n) \hat{\tau}_{k_1 k_2}(\nu - m, \omega - n) \times \exp[-i2\pi[x_{k_1}(\nu - m) + y_{k_2}(\omega - n)]] \quad (7)$$

are the aliased components that insufficient sampling folds back into the sampling passband and $\tilde{N}_{k_1 k_2}(\nu, \omega)$ is Fourier transform of the photo-detector noise. The Fourier components of the wide-sense stationary random fields $\hat{L}(\nu, \omega)$ and $\hat{N}_{k_1 k_2}(\nu, \omega)$ and the co-aliased components of the sampled scene are uncorrelated. These uncorrelated inter-relationships can be expressed as

$$E\{\hat{L}(\nu - m, \omega - n) \hat{L}^*(\nu - m', \omega - n')\} = \hat{\Phi}_L(\nu - m, \omega - n) \delta(m - m', n - n'), \quad (8)$$

$$E\{\hat{N}_{k_1 k_2}(\nu - m, \omega - n) \hat{N}_{k_1 k_2}^*(\nu - m', \omega - n')\} = \hat{\Phi}_{N_{k_1 k_2}}(\nu - m, \omega - n) \delta(m - m', n - n'), \quad (9)$$

$$E\{\hat{N}_{k_1 k_2}(\nu - m, \omega - n) \hat{N}_{l_1 l_2}^*(\nu - m', \omega - n')\} = 0, \quad (10)$$

$$E\{\hat{L}(\nu - m, \omega - n) \hat{N}_{k_1 k_2}^*(\nu - m', \omega - n')\} = 0. \quad (11)$$

The power spectral density (PSD) of the acquired digital image $s_{k_1 k_2}(x, y)$ is defined by:

$$\tilde{\Phi}_{s_{k_1 k_2}}(\nu, \omega) = E\{|\tilde{s}_{k_1 k_2}(\nu, \omega)|^2\}. \quad (12)$$

Using Eq. (8) through Eq. (11), the PSD of the degraded image can be expressed as

$$\tilde{\Phi}_{s_{k_1 k_2}}(\nu, \omega) = [\hat{\Phi}_L(\nu, \omega) |\hat{\tau}(\nu, \omega)|^2 + \hat{\Phi}_{N_{k_1 k_2}}(\nu, \omega)] * \underset{\sim}{\parallel} \parallel(\nu, \omega), \quad (13)$$

where $\hat{\Phi}_L$ is the PSD of the input scene and $\hat{\Phi}_{N_{k_1 k_2}}$ is the PSD of the noise associated with the $k_1 k_2$ th LR frame.

3 Optimal HR Grid Allocation

In our recent work,³⁰ the pixels of LR images are optimally allocated to a uniform HR grid using an approach called minimum square distance allocation (MSDA).

3.1 Minimum Square Distance Allocation

If the HR grid consists of $M_1 \times M_2$ blocks, and every block contains $K_1 \times K_2$ scenels, then the predetermined uniform HR grid subpixel shifts are $\frac{1}{K_1}$ and $\frac{1}{K_2}$ in the x and y directions, respectively, which constitutes a uniform pattern or raster. Unlike the uniform pattern, the subpixel shifts of the registered LR frames form a completely random structure. Consider

$$g = \left\{ (0, 0), \left(0, \frac{1}{K_2}\right), \dots, \left(\frac{K_1 - 1}{K_1}, \frac{K_2 - 1}{K_2}\right) \right\} \quad (14)$$

is the set of the predetermined subpixel shifts and

$$f = \{(x_0, y_0), (x_0, y_1), \dots, (x_{K_1-1}, y_{K_2-1})\} \quad (15)$$

is the set of estimated subpixel shifts of the registered LR frames. It is required then to find the optimum mapping or transformation $T: f \rightarrow g$ that converts the non-uniform subpixel shifts pattern into a uniform one. The approach here uses the Minkowski distance as a comparison metric to optimally and accurately allocate the elements of the set f to the elements of the set g with minimum distance between the corresponding points in these sets. If $P_{k_1 k_2} = \left(\frac{k_1}{K_1}, \frac{k_2}{K_2}\right) \in g$ and $k_i = 0, 1, \dots, K_i - 1$ with $i = 1$ or 2 and $Q_{l_1 l_2} = (x_{l_1}, y_{l_2}) \in f$ and $l_i = 0, 1, \dots, K_i - 1$ with $i = 1$ or 2 then the Minkowski distance of order p between $P_{k_1 k_2}$ and $Q_{l_1 l_2}$ is given by:³¹

$$d(P_{k_1 k_2}, Q_{l_1 l_2}) = \left(\left| \frac{k_1}{K_1} - x_{l_1} \right|^p + \left| \frac{k_2}{K_2} - y_{l_2} \right|^p \right)^{1/p} \quad (16)$$

Typically, the order p is usually set to 1 or 2. If we measure the Euclidean distance, we set $p = 2$ and to measure the Manhattan distance, we set $p = 1$. For simplicity and computational complexity purposes we use the Manhattan distance. Assume the HR grid is now empty, and we want to fill in the required locations, so we calculate the Manhattan distance between all the points in the set f and only one point in the set g and the point with the minimum distance should be set to this location in the HR grid. In other words, for a given point $P_{k_1 k_2} \in g$, the optimum and most close point to it in f is given by:

$$\arg \min \{d(P_{k_1 k_2}, Q_{l_1 l_2})\}_{l_i=0}^{l_i=K_i-1} \quad (17)$$

The search for the nearest location should be done in a zigzag scan to avoid misplacing the elements of the set f to the correct locations of the HR grid. If the total number of LR frames is L , then the total number of searches required to allocate all the LR frames to the HR grid is L_i .

3.2 Subpixel Shift Adjustments

Once the locations of the LR scenels to the HR grid have been determined using the MSDA method, the phase shifts of the interlaced LR frames should be spatially shifted using discrete Fourier transform shift theorem so that the interlaced LR scenels will have uniform phase-shift differences between them. If $k_1 k_2$ th LR image is $s_{k_1 k_2}(x - x_{k_1}, y - y_{k_2})$ where x_{k_1} and y_{k_2} are the estimated subpixel shifts in the x and y directions, then its representation in the spatial frequency domain $\tilde{f}_{k_1 k_2}(\nu, \omega)$ is given by:³⁰

$$\tilde{f}_{k_1 k_2}(\nu, \omega) = \tilde{s}_{k_1 k_2}(\nu, \omega) e^{-i2\pi(x_{k_1} \nu + y_{k_2} \omega)} \quad (18)$$

Also, if the determined HR grid locations are (d_{k_1}, d_{k_2}) then the subpixel shift adjustment can be performed in the spatial frequency domain by readjusting the phase of the LR image $\tilde{f}_{k_1 k_2}(\nu, \omega)$ as given by:

$$\tilde{g}_{k_1 k_2}(\nu, \omega) = \tilde{f}_{k_1 k_2}(\nu, \omega) e^{i2\pi[(x_{k_1} - d_{k_1})\nu + (y_{k_2} - d_{k_2})\omega]} \quad (19)$$

3.3 HR Grid Interlacing

After the phase shifts of the individual LR images have been corrected, the reconstruction of the output image is performed by interlacing the pixels of the acquired images into a HR grid with a sampling density equals $K_1 K_2$ times the sampling density of the individual LR images. Thus the composite HR image S is given by:

$$S(K_1 m_1 + k_1, K_2 m_2 + k_2) = s_{k_1 k_2}(m_1, m_2), \quad (20)$$

and its Fourier transform is give by:

$$\begin{aligned} \tilde{S}(\nu, \omega) &= \frac{1}{K_1 M_1 K_2 M_2} \sum_{m_1=0}^{K_1 M_1 - 1} \sum_{m_2=0}^{K_2 M_2 - 1} S(m_1, m_2) \\ &\times \exp \left[-i2\pi \left(\frac{\nu m_1}{K_1 M_1} + \frac{\omega m_2}{K_2 M_2} \right) \right]. \end{aligned} \quad (21)$$

The above equation can be rewritten and simplified as

$$\begin{aligned} \tilde{S}(\nu, \omega) &= \frac{1}{K_1 K_2} \sum_{k_1=0}^{K_1-1} \sum_{k_2=0}^{K_2-1} \frac{1}{M_1 M_2} \\ &\times \sum_{m_2=0}^{M_2-1} \sum_{m_1=0}^{M_1-1} S(K_1 m_1 + k_1, K_2 m_2 + k_2) \\ &\times \exp \left[-i2\pi \nu \left(\frac{K_1 m_1 + k_1}{K_1 M_1} \right) \right] \\ &\times \exp \left[-i2\pi \omega \left(\frac{K_2 m_2 + k_2}{K_2 M_2} \right) \right]. \end{aligned} \quad (22)$$

Rearranging the summation terms

$$\begin{aligned} \tilde{S}(\nu, \omega) &= \frac{1}{K_1 K_2} \sum_{k_1=0}^{K_1-1} \sum_{k_2=0}^{K_2-1} \frac{1}{M_1 M_2} \sum_{m_2=0}^{M_2-1} \sum_{m_1=0}^{M_1-1} s_{k_1 k_2}(m_1, m_2) \\ &\times \exp \left[-i2\pi \nu \left(\frac{K_1 m_1 + k_1}{K_1 M_1} \right) \right] \\ &\times \exp \left[-i2\pi \omega \left(\frac{K_2 m_2 + k_2}{K_2 M_2} \right) \right] \\ &= \frac{1}{K_1 K_2} \sum_{k_1=0}^{K_1-1} \sum_{k_2=0}^{K_2-1} \left\{ \frac{1}{M_1 M_2} \sum_{m_1=0}^{M_1-1} \sum_{m_2=0}^{M_2-1} s_{k_1 k_2}(m_1, m_2) \right. \\ &\times \exp \left[-i2\pi \left(\frac{\nu m_1}{M_1} + \frac{\omega m_2}{M_2} \right) \right] \left. \right\} \\ &\times \exp \left[-i2\pi \left(\frac{\nu k_1}{K_1 M_1} + \frac{\omega k_2}{K_2 M_2} \right) \right]. \end{aligned} \quad (23)$$

Recall that the discrete Fourier transform of the degraded image $\tilde{s}_{k_1 k_2}$ is given by

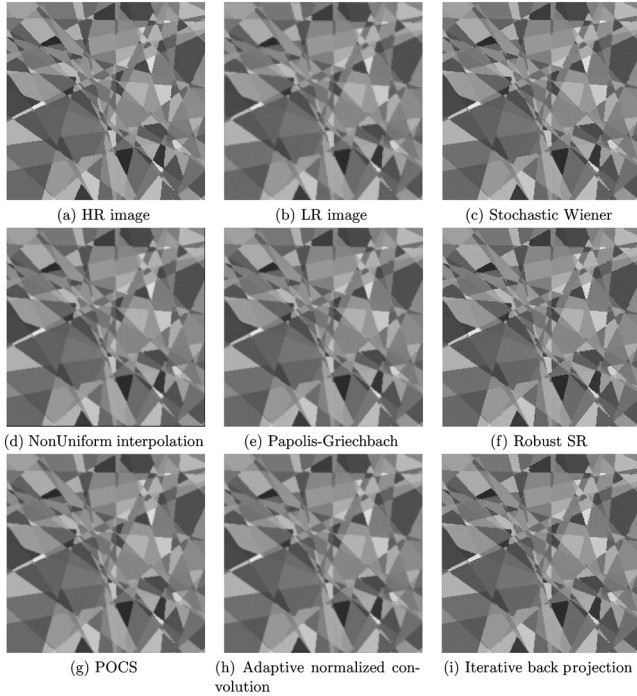


Fig. 2 Different full-SR reconstructed images ($\sigma = 0.7$ and $\text{SNR} = 32$).

$$\begin{aligned} \tilde{s}_{k_1 k_2}(\nu, \omega) &= \frac{1}{M_1 M_2} \sum_{m_1=0}^{M_1-1} \sum_{m_2=0}^{M_2-1} s_{k_1 k_2}(m_1, m_2) \\ &\quad \times \exp \left[-i2\pi \left(\frac{\nu m_1}{M_1} + \frac{\omega m_2}{M_2} \right) \right]. \end{aligned} \quad (24)$$

So, by substituting Eq. (24) into Eq. (23), the Fourier transform of the reconstructed image $\tilde{S}(\nu, \omega)$ can be expressed as

$$\begin{aligned} \tilde{S}(\nu, \omega) &= \frac{1}{K_1 K_2} \sum_{k_1=0}^{K_1-1} \sum_{k_2=0}^{K_2-1} \tilde{s}_{k_1 k_2}(\nu, \omega) \\ &\quad \times \exp \left[-i2\pi \left(\frac{\nu k_1}{M_1 K_1} + \frac{\omega k_2}{M_2 K_2} \right) \right]. \end{aligned} \quad (25)$$

If x_{k_1} and y_{k_2} are the subpixel shifts in the x and y directions respectively and (ν', ω') is the normalized frequency pair then the last equation can be written as

$$\begin{aligned} \tilde{S}(\nu', \omega') &= \frac{1}{K_1 K_2} \sum_{k_1=0}^{K_1-1} \sum_{k_2=0}^{K_2-1} \tilde{s}_{k_1 k_2}(\nu', \omega') \\ &\quad \times \exp \left[-i2\pi (\nu' x_{k_1} + \omega' y_{k_2}) \right]. \end{aligned} \quad (26)$$

Thus, the reconstructed image in the frequency domain is the sum of the phase-shifted Fourier transform of the individual scans.³²

4 Derived Stochastic Wiener Restoration Filter

In this section, we derive the stochastic Wiener filter constrained by the periodic and nonperiodic interrelationships between the different frequency components of the proposed

SR system. It can be used as reconstruction filter as well as a restoration filter to recover images from the degradations that are introduced during image acquisition and image display. If the number of LR frames is $K_1 K_2$, which is sufficient to produce full SR along the horizontal and vertical dimensions of the reconstructed images, then the derived filter works only as a restoration filter. On the other hand, if the available number of LR images is less than $K_1 K_2$, then the filter works as a restoration and a reconstruction filter to estimate missing pixels on the dense HR grid. In spatial domain, the observed image $R_o(x, y)$ is reconstructed through the spatial convolution of the Wiener filter $\Psi(x, y)$, the spatial response of the image-display device $\tau_d(x, y)$ and the interlaced image $S(x, y)$ as given by

$$R_o(x, y) = S(x, y) * \Psi(x, y) * \tau_d(x, y). \quad (27)$$

The spatial frequency representation of this equation is given by

$$\hat{R}_o(\nu, \omega) = \tilde{S}(\nu, \omega) \hat{\Psi}(\nu, \omega) \hat{\tau}_d(\nu, \omega). \quad (28)$$

By substituting Eqs. (6) and (26) into Eq. (28), the output image \hat{R}_o can be decomposed into three components as defined by

$$\hat{R}_o(\nu, \omega) = \hat{R}_f(\nu, \omega) + \hat{R}_a(\nu, \omega) + \hat{R}_n(\nu, \omega), \quad (29)$$

where \hat{R}_f is the filtered component that accounts for the low-pass filtering of the image gathering, image display devices, and the restoration filter and it is given by

$$\begin{aligned} \hat{R}_f(\nu, \omega) &= \frac{1}{K_1 K_2} \sum_{k_1 k_2} \hat{L}(\nu, \omega) \hat{\tau}_{k_1 k_2}(\nu, \omega) \\ &\quad \times \exp \left[-i4\pi (\nu x_{k_1} + \omega y_{k_2}) \right] \hat{\tau}_d(\nu, \omega) \hat{\Psi}(\nu, \omega), \end{aligned} \quad (30)$$

where $\hat{R}_n(\nu, \omega)$ is the noise component that accounts for the additive white noise and is given by

$$\begin{aligned} \hat{R}_n(\nu, \omega) &= \frac{1}{K_1 K_2} \sum_{k_1 k_2} \tilde{N}_{k_1 k_2}(\nu, \omega) \exp \left[-i4\pi (\nu x_{k_1} + \omega y_{k_2}) \right] \\ &\quad \times \hat{\tau}_d(\nu, \omega) \hat{\Psi}(\nu, \omega), \end{aligned} \quad (31)$$

and $\hat{R}_a(\nu, \omega)$ is the aliasing component that accounts for the frequency folding due to sampling beyond the Nyquist rate, and it is given by

$$\begin{aligned} \hat{R}_a(\nu, \omega) &= \frac{1}{K_1 K_2} \sum_{k_1 k_2} \hat{N}_a(\nu, \omega) \exp \left[-i4\pi (\nu x_{k_1} + \omega y_{k_2}) \right] \\ &\quad \times \hat{\tau}_d(\nu, \omega) \hat{\Psi}(\nu, \omega), \end{aligned} \quad (32)$$

where $\hat{N}_a(\nu, \omega)$ is defined in Eq. (7). The Wiener filter minimizes the mean-square restoration error (MSRE) e^2 between the input scene $L(x, y)$ and the output image $R_o(x, y)$, as defined by²⁹

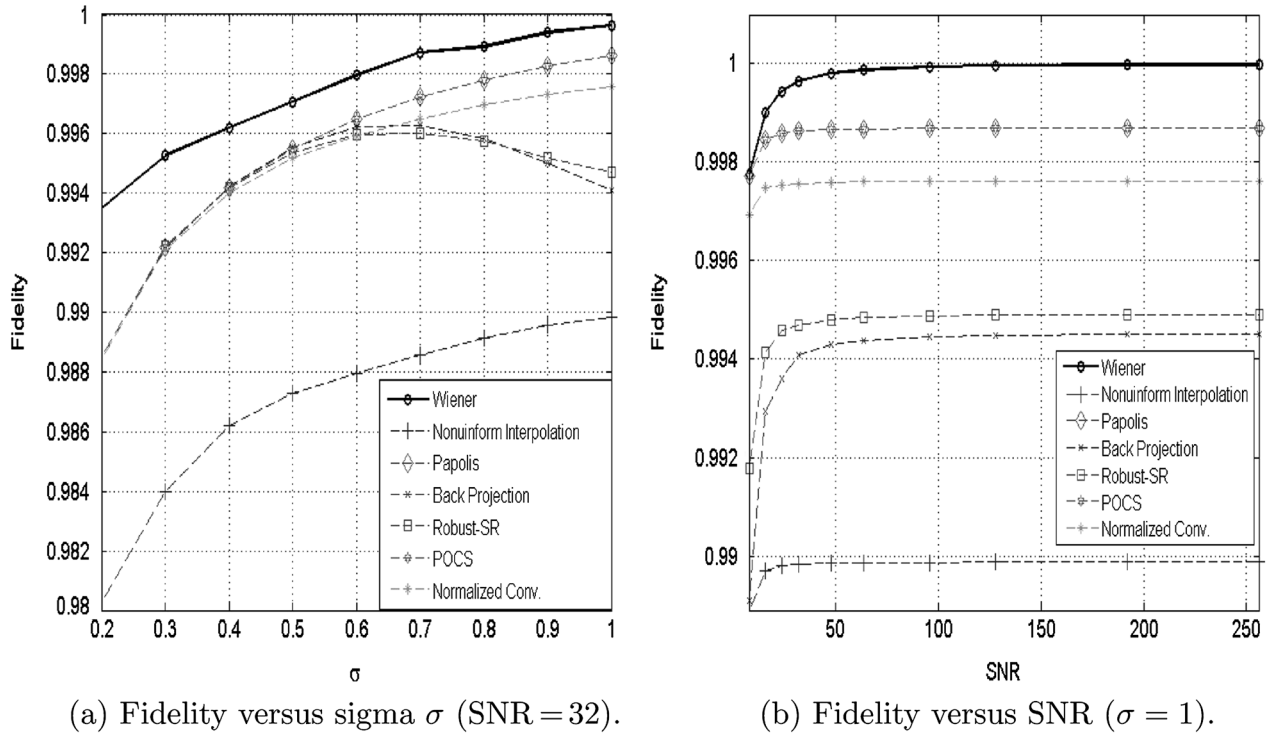


Fig. 3 Fidelity comparison for different full-SR reconstructed images.

$$\begin{aligned}
 e^2 &= E \left\{ \iint |L(x, y) - R_o(x, y)|^2 dx dy \right\} \\
 &= E \left\{ \iint |\hat{L}(\nu, \omega) - \tilde{S}(\nu, \omega) \hat{\Psi}(\nu, \omega) \hat{\tau}_d(\nu, \omega)|^2 d\nu d\omega \right\}.
 \end{aligned} \tag{33}$$

Using Eq. (8) through Eq. (11), the optimal Wiener filter that minimizes the MSRE is given by:

$$\hat{\Psi}(\nu, \omega) = \frac{\hat{\Phi}_{L^S}(\nu, \omega) \hat{\tau}_d^*(\nu, \omega)}{\hat{\Phi}_S(\nu, \omega) |\hat{\tau}_d(\nu, \omega)|^2}, \tag{34}$$

where $\hat{\Phi}_{L^S}(\nu, \omega)$ is the cross power-spectrum between the input scene, and the reconstructed image and $\hat{\Phi}_S(\nu, \omega)$ is the power spectrum density of the reconstructed image. If the photo-detector noise is modeled as wide-sense stationary discrete random process, then Wiener filter can be expressed as a function of the SNR σ_L/σ_N as given by

$$\hat{\Psi}(\nu, \omega) = \frac{K_1 K_2 \hat{\Phi}'_L(\nu, \omega) \sum_{k_1 k_2} \hat{\tau}_{k_1 k_2}^*(\nu, \omega) \hat{\tau}_d^*(\nu, \omega) \exp [i4\pi(\nu x_{k_1} + \omega y_{k_2})] / |\hat{\tau}_d(\nu, \omega)|^2}{\hat{\Phi}'_L(\nu, \omega) * \left| \sum_{mn} \left| \sum_{k_1 k_2} |\hat{\tau}_{k_1 k_2}^*(\nu', \omega')|^2 \exp [-i2\pi(\nu' x_{k_1} + \omega' y_{k_2})] \right|^2 + \sum_{k_1 k_2} (\sigma_L / \sigma_{N_{k_1 k_2}})^{-2} \right|}, \tag{35}$$

where σ_L and σ_N are the variance of the input scene and the noise respectively, $\hat{\Phi}'_L(\nu, \omega) = \sigma_L^{-2} \hat{\Phi}_L(\nu, \omega)$, $\nu' = 2\nu - m$ and $\omega' = 2\omega - n$. It can be seen that Wiener filter is a function of the different components of the CDC system, the subpixel shifts of the individual LR frames and the system SNR.

5 Simulations and Results

We started with a HR image to simulate the continuous input scene, and then we lower its quality to simulate the degradations that are encountered during the image acquisition process such as blurring, aliasing, and noise. Also, during our

simulations we consider two different cases: (1) LR images are sufficient to reconstruct a full-SR image in the vertical and horizontal dimensions and (2) LR images are insufficient to reconstruct partial-SR image. We compare the performance of our method with some of the well known SR reconstruction approaches in terms of fidelity, visual quality assessment, and the computational time. These techniques are nonuniform interpolation, Papoulis-Gerchberg,³³ iterated back projection,²⁴ robust SR,³⁴ POCS,²¹ and structure-adaptive normalized convolution.³⁵ All of these algorithms were developed at the Laboratory of Audiovisual Communications (LCAV), Ecole Polytechnique Federale de Lausanne (EPFL), Switzerland.³⁶

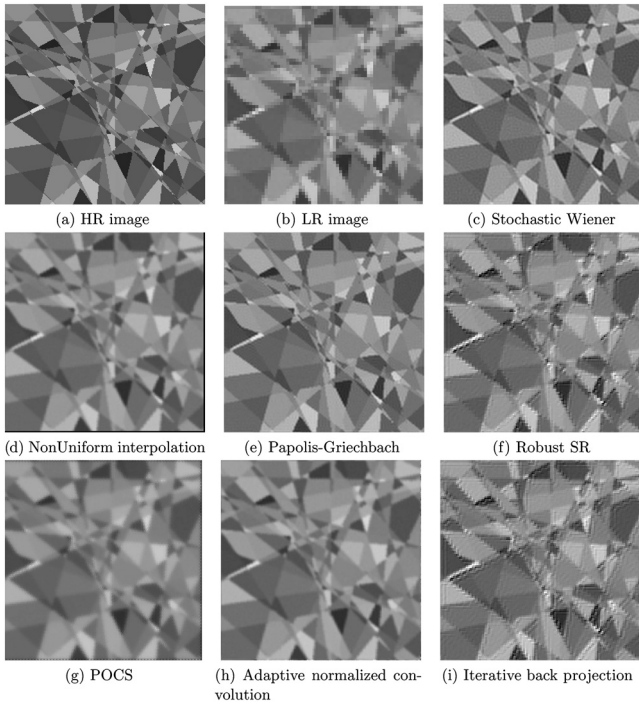


Fig. 4 Different partial-SR reconstructed images ($\sigma = 0.7$ and SNR = 32).

5.1 Simulated Images

Consider a 256×256 simulated random polygon image. The boundaries of the random polygon image are distributed according to Poisson probability with a mean separation μ and whose input scene magnitudes are distributed according to independent zero-mean Gaussian statistics of variance σ_L^2 . The mean separation μ is measured relative to the sampling

interval of the image-gathering device and treated as the mean spatial detail of the scene.⁸ In our simulations, the random polygon has mean spatial detail of 3. The random polygon image is blurred by a Gaussian lowpass filter defined by

$$\hat{\tau}(\nu, \omega) = \exp \left[-\frac{\nu^2 + \omega^2}{\sigma^2} \right], \tag{36}$$

where σ is the optical-response index for which $\hat{\tau}(\nu, \omega) \approx 0.37$. This Gaussian filter approximates the SFR of the image-gathering device. Schade³⁷ and Schreiber³⁸ concluded that the image-gathering device with a SFR $\hat{\tau}(\nu, \omega)$ characterized by $\sigma = 0.8$ provides generally the most favorable trade-off between sharpness and aliasing artifacts without the aid of digital processing. A white noise is superimposed to the image with a given SNR defined by:

$$\text{SNR} = 10 \log_{10} \left(\frac{\sigma_L^2}{\sigma_N^2} \right), \tag{37}$$

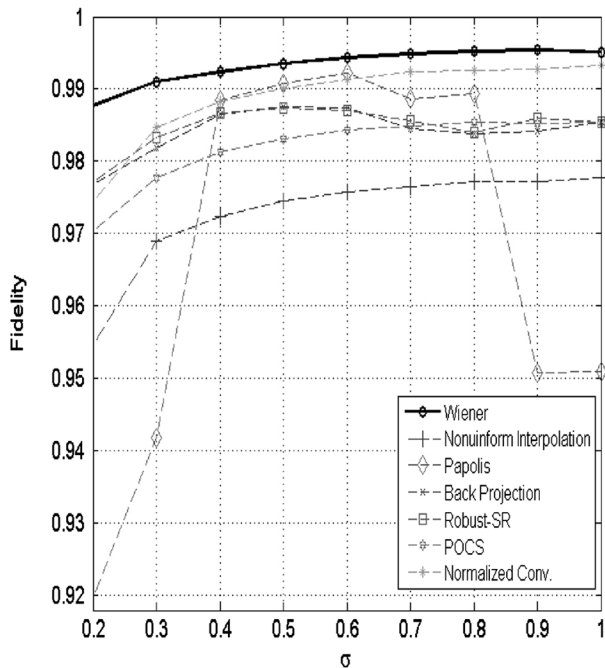
where σ_L^2 is the variance of the image scene, and σ_N^2 is the variance of the white noise. The derivation of the Weiner restoration filter depends on the estimation of the input scene PSD $\hat{\Phi}_L$. Itakura et al.³⁹ have shown that the PSD of natural scenes can be approximated by:

$$\hat{\Phi}_L(\nu, \omega) = \frac{2\pi\mu^2\sigma_L^2}{[1 + (2\pi\mu\rho)^2]^{3/2}}, \tag{38}$$

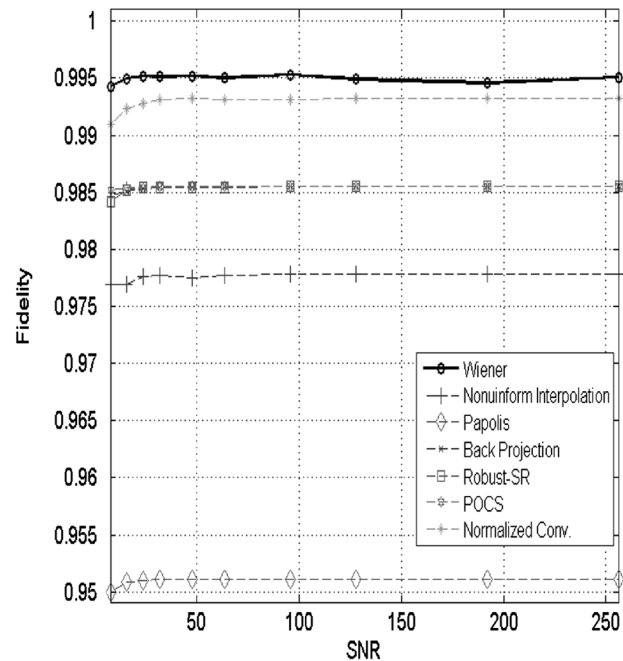
where $\rho^2 = \nu^2 + \omega^2$ and μ is the scene mean spatial detail.

5.1.1 Case 1: Full-SR

In this case the blurred and noisy image is sampled at half-pixel location resulting in four images of dimensions



(a) Fidelity versus sigma σ (SNR = 32).



(b) Fidelity versus SNR ($\sigma = 1$).

Fig. 5 Fidelity comparison for different partial-SR reconstructed images.

128 × 128. These images are used to reconstruct the SR images using the derived Wiener filter in addition to the other mentioned SR reconstruction algorithms. Figure 2 shows the reconstructed SR images using different SR approaches for $\sigma = 0.7$ and SNR = 32. It can be seen that all of them is better than the LR image given in Fig. 2(b). Also, the Wiener reconstructed SR image is very close to the original HR image and is much better than the other reconstructed images. In addition, to compare the visual quality of the reconstructed images, we examine the fidelity between the different reconstructed images and the original simulated scene against either the optical response with a fixed SNR = 32 or SNR with a fixed $\sigma = 1$. The results can be seen in Figs. 3(a) and 3(b). The fidelity of the Wiener reconstructed images is greater than the fidelities of the other reconstructed images. Also, the fidelity is improved when the optical response index is increased. This is because when the optical index is decreasing, the reconstructed image will lose some of its high-frequency content, which will be reflected on its visual quality and its fidelity.

5.1.2 Case 2: Partial-SR

Here the blurred and noisy image is sampled at quarter-pixel location resulting in 16 images of dimensions 64 × 64. We select four of them to reconstruct the SR images using the same procedure described in the first case. Figure 4 shows the reconstructed SR images using different SR approaches for $\sigma = 0.7$ and SNR = 32. It can be seen that all the reconstructed SR images are blurrier than the full-SR reconstructed images due to the interpolation and reconstruction processes. Also, all the reconstructed images are better than the LR image given in Fig. 4(b). The Wiener reconstructed SR image is close to the original HR image and is much better than the other reconstructed images. Figures 5(a) and 5(b) show a fidelity comparison between different SR reconstructed images when changing either the SNR and keep σ at 0.7 or changing σ and keep SNR at 32. Similarly, the fidelity of the Wiener reconstructed image is greater than the fidelities of the other reconstructed images, and it is improved when the optical response index is increased.

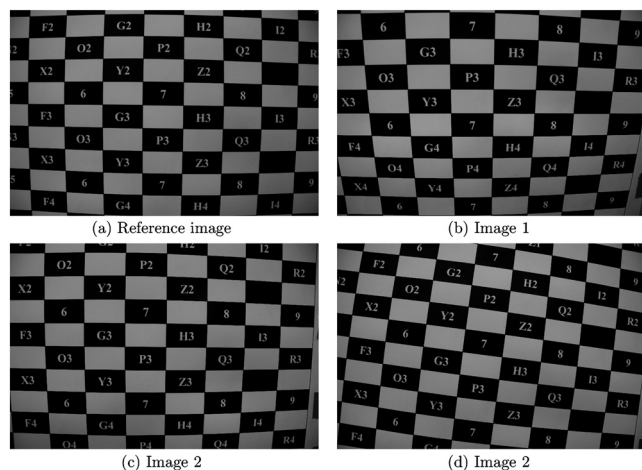


Fig. 6 Different captured checkerboard images.

Table 1 Estimated subpixel shifts.

	Subpixel shifts	
	x-direction	y-direction
Image 1	-0.01	-0.06
Image 2	-0.03	-0.03
Image 3	-0.04	-0.03

Table 2 Adjusted subpixel shifts.

Image	New subpixel shift
Reference image	(0.5, 0.5)
Image 1	(0.5, 0)
Image 2	(0, 0.5)
Image 3	(0, 0)

5.2 Real Images

SR reconstructions in real applications have many challenging problems. It is crucial to accurately estimate the subpixel shifts of LR images as they have a great impact on the reconstruction of SR images. Also, estimating the optical blur caused by system optics and the noise caused by photo-detectors greatly affect the restoration process, which in turn affects the visual quality of the reconstructed and restored images. Throughout our work we assume that the blur and noise are already known, and we are concerned with

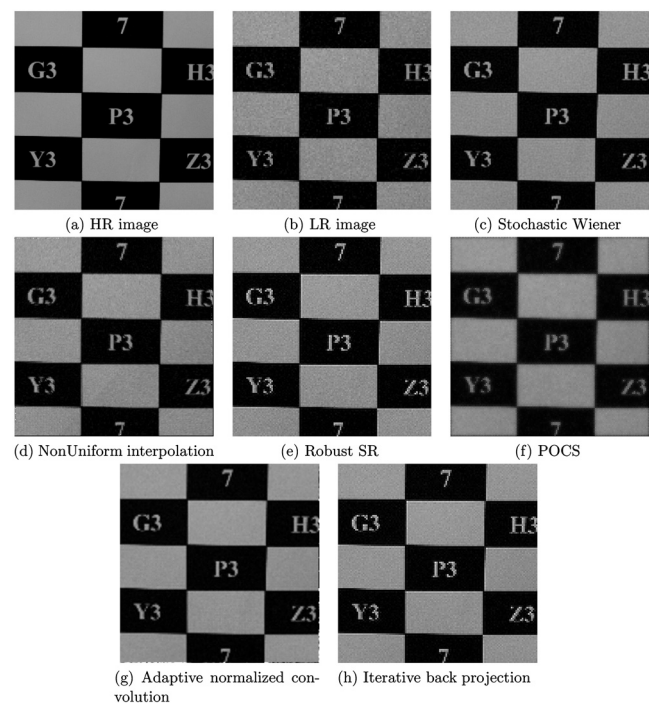


Fig. 7 Different full-SR reconstructed checkerboard images ($\sigma = 0.8$ and SNR = 128).

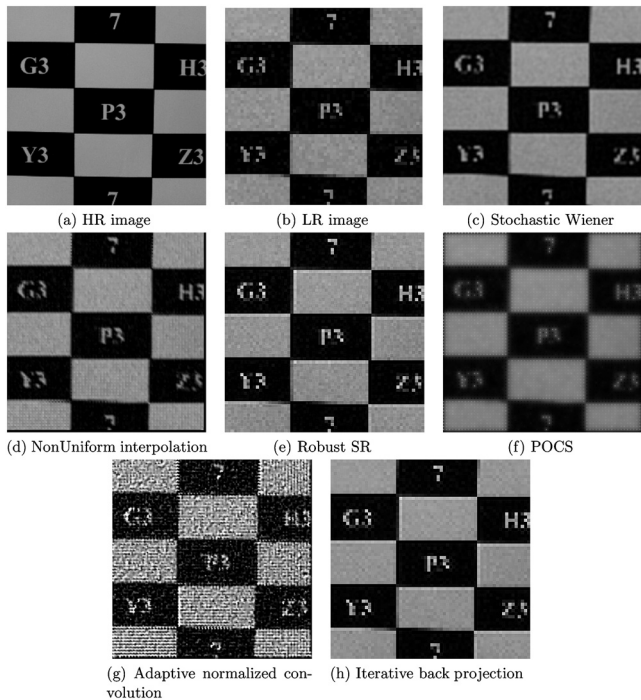


Fig. 8 Different partial-SR reconstructed checkerboard images ($\sigma = 0.8$ and $SNR = 128$).

the accurate estimation of the subpixel shifts and their optimal allocation to the HR grid as presented in our recent work.³⁰ This optimal allocation depends on readjusting the subpixel shifts of LR images to match a uniformly spaced pattern using a minimum square approach and Fourier transform shift property. In our experiments, we capture a set of checkerboard images. By controlling the camera tripod, we collect a set of images of dimensions 1280×1280 that have slightly different looks of the same scene. Figure 6 shows a set of these captured images.

Through out the simulations, we neglect the effect of the camera blur and noise and subsample the acquired

images to 256×256 , which will be used for the quantitative assessment of SR reconstruction and restoration. Then degradations are superimposed to the images as we did in the random polygon images. The images will be subsampled at quarter and half pixel locations to examine both partial-SR and full-SR cases, respectively. The degraded images will be registered with respect to a reference image to a sub-pixel precision. Table 1 lists the estimated subpixel shifts between the different images and the reference one, and it can be seen that they are random and do not follow a uniform pattern. They will be adjusted and optimally mapped to a uniform HR grid, which is listed in Table 2. The Wiener filter is applied to the composed HR grid, and a comparison between its output and the different SR approaches outputs is displayed in Figs. 7 and 8 for the full and partial-SR cases, respectively. Images with full SR have better visual quality and sharpness than the ones with partial SR. Also, the images with Wiener restoration are much better than the other techniques in both the cases of full and partial SR. Comparisons between the fidelity for the different SR reconstruction techniques are listed in Table 3 for full-SR and partial-SR cases. Images with Wiener restoration have higher fidelity than the other techniques. In addition, full-SR images have higher fidelities than partial-SR images.

5.3 Computational Costs

The computational costs of the different SR techniques are listed in Table 4. The simulations are performed using MATLAB 7.8 Release 2009a program on OPTIPLEX 780 (Intel^(R) Core (TM)2 Quad 2.66 GHz CPU, 8.00 GB RAM, MS Windows 7 Professional 2009). The performance of the different SR techniques in case of partial SR is much faster than that in case of full SR. Also, Wiener computational time is much smaller than the other SR techniques. Most of Wiener computational time is consumed in a preprocessing step (0.355 s in case of partial SR and 0.78 s in case of full SR), which is considered as the main demerit of this approach. In a future work, we shall focus on reducing this computational time by working on smaller blocks of the

Table 3 Fidelity comparison for different reconstructed SR images.

SR Techniques	Stochastic Wiener	Non-uniform interpolation	Robust SR	POCS	Adaptive normalized convolution	Iterative back projection
Full-SR	0.984	0.953	0.963	0.956	0.96	0.964
Partial-SR	0.927	0.852	0.896	0.875	0.623	0.898

Table 4 Computational time for full-SR reconstructed SR images.

SR Techniques	Stochastic Wiener	Non-uniform interpolation	Robust SR	POCS	Adaptive normalized convolution	Iterative back projection
Full-SR	0.92	2.839	36.56	13.665	11.716	13.713
Partial-SR	0.434	0.96	35.319	12.616	7.176	5.756

reconstructed image, and hence the required time for preparing the Wiener filter is reduced.

6 Conclusions and Future Work

In this paper, we present a derivation of the stochastic Wiener filter for the general SR reconstruction problem. Traditional developments of Wiener filter in the field of image processing are based on the assumption that the image gathering device is constrained solely by blurring and noise, and those developments fail to account for the insufficient sampling that results in aliasing presented in the acquired images. While others extended this filter for microscanning reconstruction, where subpixel shifts between acquired images are known and constitute a uniform grid, our derivation is based on a CDC system model that represents most of the degradations encountered during the acquisition-display processes. We generalize the derivation for the general SR problem by readjusting subpixel shifts of individual frames and optimally allocate their pixels to the HR grid. Wiener SR reconstructed images have a pleasant, sharp visual quality with a maximum obtainable fidelity. The reconstructed images are preferable to the other SR reconstructed images using different SR approaches. It is possible to improve the visual quality of the reconstructed images depending on the availability of sufficient LR frames. Simulation results show that images with full-SR are both better and sharper than the ones with partial-SR. Although the stochastic Wiener approach outperforms the other approaches, its computational complexity is still high and needs to be reduced without sacrificing the maximum obtainable fidelity and the pleasant visual quality of the reconstructed images, which is our future work.

A part of this work was presented in SPIE Optics and Photonics⁴⁰ conference.

Acknowledgments

The authors wish to thank the NASA Aviation Safety Program for the funding, which made this work possible. A significant portion of the work was supported under the NASA cooperative agreement NNL07AA02A with ODU. The authors deeply cherish the memory of Dr. Rahman and his outstanding contribution to this study.

References

1. S. C. Park, M. K. Park, and M. G. Kang, "Super-resolution image reconstruction: a technical overview," *IEEE Sig. Process. Mag.* **20**(3), 21–36 (2003).
2. J. Shi, S. E. Reichenbach, and J. D. Howe, "Small-kernel superresolution methods for microscanning imaging systems," *Appl. Opt.* **45**(6), 1203–1214 (2006).
3. M. K. Ng and A. C. Yau, "Super-resolution image restoration from blurred low-resolution images," *J. Math. Imag. Vis.* **23**(12), 262–271 (2005).
4. S. Borman and R. Stevenson, "Spatial resolution enhancement of low-resolution image sequences: a comprehensive review with directions for future research," tech. rep., Department of Electrical Engineering, University of Notre Dame, Notre Dame, Indiana, USA (July 1998).
5. Q. Tian and M. N. Huhns, "Algorithms for subpixel registration," *Comput. Vis. Graph. Image Process.* **35**(14), 220–233 (1986).
6. M. Guizar-Sicairos, S. T. Thurman, and J. R. Fienup, "Efficient subpixel image registration algorithms," *Opt. Lett.* **33**(2), 156–158 (2008).
7. R. A. Reed, "Comparison of subpixel phase correlation methods for image registration," final report, Aerospace Testing Alliance, Arnold Air Force Base, Tennessee, USA (2010).
8. F. O. Huck, C. L. Fales, and Z. Ur Rahman, *Visual Communications: An Information Theory Approach*, 1st Ed., Kluwer Academic Publishers, Boston, Mass (1997).
9. A. K. Katsaggelos, *Digital Image Restoration*, 1st Ed., Springer-Verlag, New York (1991).
10. A. Bovik, Ed., "Basic methods for image restoration and identification," *Handbook of Image and Video Processing*, pp. 167–173, 1st Ed., Academic Press, Burlington, MA (2000).
11. M. Alam et al., "Infrared image registration and high-resolution reconstruction using multiple translationally shifted aliased video frames," *IEEE Trans. Instrum. Meas.* **49**(5), 915–923 (2000).
12. R. C. Gonzalez and R. E. Woods, *Digital Image Processing*, 2nd Ed., Prentice Hall, New Jersey (2002).
13. H. Ur and D. Gross, "Improved resolution from subpixel shifted pictures," *CVGIP: Graph. Models Image Process.* **54**(2), 181–186 (1992).
14. T. Komatsu et al., "Signal-processing based method for acquiring very high resolution images with multiple cameras and its theoretical analysis," *IEE Proc. I Comm. Speech and Vision*, Vol. **140**, pp. 19–24 (February 1993).
15. N. Shah and A. Zakhor, "Resolution enhancement of color video sequences," *IEEE Trans. Image Process.* **8**(6), 879–885 (1999).
16. N. Nguyen and P. Milanfar, "A wavelet-based interpolation-restoration method for superresolution (wavelet superresolution)," *Circ. Syst. Signal Process.* **19**(4), 321–338 (2000).
17. R. Y. Tsai and T. S. Huang, Eds., "Multiframe image restoration and registration," in *Advances in Computer Vision and Image Processing*, pp. 317–339, JAI Press, Greenwich, CT (1984).
18. S. Kim, N. Bose, and H. Valenzuela, "Recursive reconstruction of high resolution image from noisy undersampled multiframe," *IEEE Trans. Acoust. Speech Signal Process.* **38**(6), 1013–1027 (1990).
19. S. Kim and W.-Y. Su, "Recursive high-resolution reconstruction of blurred multiframe images," *IEEE Trans. Image Process.* **2**(4), 534–539 (1993).
20. H. E. Sankaran, "Super-resolution using nonuniform to uniform resampling in spline spaces," master of science, Tamere University of Technology, Tampere, Finland (2007).
21. K. Sauer and J. Allebach, "Iterative reconstruction of bandlimited images from nonuniformly spaced samples," *IEEE Trans. Circ. Syst.* **34**(12), 1497–1506 (1987).
22. H. Stark and P. Oskoui, "High-resolution image recovery from image-plane arrays, using convex projections," *J. Opt. Soc. Am. A* **6**(11), 1715–1726 (1989).
23. A. Patti, M. Sezan, and A. Murat Tekalp, "Superresolution video reconstruction with arbitrary sampling lattices and nonzero aperture time," *IEEE Trans. Image Process.* **6**(8), 1064–1076 (1997).
24. M. Irani and S. Peleg, "Improving resolution by image registration," *CVGIP: Graph. Models Image Process.* **53**(3), 231–239 (1991).
25. N. Nguyen, P. Milanfar, and G. Golub, "A computationally efficient superresolution image reconstruction algorithm," *IEEE Trans. Image Process.* **10**(4), 573–583 (2001).
26. S. Farsiu et al., "Fast and robust multiframe super resolution," *IEEE Trans. Image Process.* **13**(10), 1327–1344 (2004).
27. M. Elad and A. Feuer, "Super-resolution reconstruction of an image," in *The 19th IEEE Conference*, pp. 391–394, Jerusalem, Israel (1996).
28. M. Elad and A. Feuer, "Restoration of a single superresolution image from several blurred, noisy, and undersampled measured images," *IEEE Trans. Image Process.* **6**(12), 1646–1658 (1997).
29. C. L. Fales et al., "Wiener restoration of sampled image data: end-to-end analysis," *J. Opt. Soc. Am. A* **5**(3), 300–314 (1988).
30. A. H. Yousef, Z. ur Rahman, and M. Karim, "On the restoration of the microscanned images captured from unmanned airborne vehicles," *Proc. SPIE* **8056**, 80560D (2011).
31. A. R. Webb, *Statistical Pattern Recognition*, 2nd Ed., John Wiley & Sons, Chichester, UK (2002).
32. M. R. Idema, "Sub-pixel techniques to improve spatial resolution," Ph.D. thesis William & Mary College, Williamsburg, Virginia (2001).
33. P. Chatterjee et al., "Application of Papoulis-Gerchberg method in image super-resolution and inpainting," *Comput. J. (Switzerland)* **52**(1), 80–89 (2009).
34. A. Zomet, A. Rav-Acha, and S. Peleg, "Robust super-resolution," in *Proc. International Conf. on Computer Vision and Pattern Recognition (CVPR)*, Hawaii (2001).
35. T. Pham, L. van Vliet, and K. Schutte, "Robust fusion of irregularly sampled data using adaptive normalized convolution," *EURASIP J. Appl. Sig. Process.* **2006**(8), 236–247 (2006).
36. P. Vandewalle, K. Krichane, and P. Zbinden, "Superresolution-graphical user interface," <http://lcav.epfl.ch/software/superresolution> (2006), (14 April 2011).
37. S. O. H. Schade, "Image gradation, graininess and sharpness in television and motion-picture systems," *J. Soc. Motion Pict. Telev. Eng.* **56**(2), 137–174 (1951).
38. W. F. Schreiber, *Fundamentals of Electronic Imaging Systems*, 3rd Ed., Springer-Verlag, Berlin (1993).
39. Y. Itakura, S. Tsutsumi, and T. Takagi, "Statistical properties of the background noise for the atmospheric windows in the intermediate infrared region," *Infrared Phys.* **14**(1), 17–29 (1974).
40. A. H. Yousef, J. Li, and M. Karim, "On the visual quality enhancement of super-resolution images," *Proc. SPIE* **8135**(1), 81350Z (2011).



Amr Yousef graduated with BSc in electrical engineering and MSc in engineering mathematics from Alexandria University, Egypt, in 2001 and 2006 respectively. He joined the Computational Intelligence and Vision Lab at Old Dominion University (ODU) in 2008 for a PhD. His research is in image processing focusing on super-resolution reconstruction and restoration techniques. He is a student member of SPIE and OSA.



Dr. Jiang Li received his Phin electrical engineering from the University of Texas at Arlington, Texas, in 2004, an MS degree in automation from Tsinghua University, China, in 2000, and a BS in electrical engineering from Shanghai Jiaotong University, China, in 1992. His research interests include machine learning, computer-aided medical diagnosis systems, medical signal/image processing, neural network, and modeling and simulation. Dr. Li worked as a postdoctoral

fellow at the department of radiology, National Institutes of Health, from 2004 to 2006. He joined ODU as an assistant professor in spring 2007. He is also affiliated with Virginia Modeling, Analysis, and Simulation Center (VMASC). He is a member of the IEEE and the Sigma Xi.



Mohammad A. Karim is vice president for research of ODU. He is North American Editor of *Optics and Laser Technology*, an associate editor of *IEEE Transactions on Education*, and a member of the Editorial Boards of *Microwave and Optical Technology Letters* and *World Journal of Modeling and Simulation*. He is an elected fellow of the Optical Society of America (OSA), the Society of Photo-Instrumentation Engineers (SPIE), the Institute of Electrical and Electronics Engineers (IEEE), the Institute of Physics (InstP), the Institution of Engineering and Technology (IET), and the Bangladesh Academy of Sciences.